

FEATURE ARTICLE

Self-Assembly at the Liquid/Solid Interface: STM Reveals

Steven De Feyter* and Frans C. De Schryver*

*Department of Chemistry, Laboratory of Photochemistry and Spectroscopy, Katholieke Universiteit Leuven, Celestijnenlaan 200-F, 3001 Leuven, Belgium**Received: October 14, 2004; In Final Form: December 24, 2004*

The liquid/solid interface provides an ideal environment to investigate self-assembly phenomena, and scanning tunneling microscopy (STM) is the preferred methodology to probe the structure and the properties of physisorbed monolayers on the nanoscale. Physisorbed monolayers are of relevance in areas such as lubrication, patterning of surfaces on the nanoscale, and thin film based organic electronic devices, to name a few. It's important to gain insight in the factors which control the ordering of molecules at the liquid/solid interface in view of the targeted properties. STM provides detailed insight into the importance of molecule-substrate (epitaxy) and molecule-molecule interactions (hydrogen bonding, metal complexation, and fluorophobic/fluorophilic interactions) to direct the ordering of both achiral and chiral molecules on the atomically flat surface. By controlling the location and orientation of functional groups, chemical reactions can be induced at the liquid/solid interface, via external stimuli, such as light, or by controlled manipulation with the STM tip. The electronic properties of the self-assembled physisorbed molecules can be probed by taking advantage of the operation principle of STM, revealing spatially resolved intramolecular differences within these physisorbed molecules.

Introduction

Control of the lateral assembly and spatial arrangement of micro- and nanoobjects at interfaces is often a prerequisite when it comes to potential applications in the field of nanoscience and technology. To create two-dimensional (2D) patterns, one can take advantage of “active” manipulation techniques such as photolithography or electron beam lithography¹ and “soft lithography” techniques.² Scanning probe microscopy (SPM) techniques, such as scanning tunneling microscopy (STM) and atomic force microscopy (AFM), are another class of techniques, which can be implemented for the controlled manipulation of matter.^{3–9} Self-assembly methods provide an alternative approach to make defined structures with dimensions on the nanometer scale. Self-assembly is a natural phenomenon, which can be observed in many biological, chemical, and physical processes.¹⁰ A textbook example of self-assembly on surfaces is the spontaneous formation of chemisorbed self-assembled monolayers (SAMs),¹¹ typically thiols on gold.^{12,13} Chemisorption renders the modified substrate properties which differ significantly from the “naked” substrate, which makes these chemisorbed self-assembled monolayers of prime interest for technological applications. Modification of the exposed groups at the monolayer/air interface leads to a wealth of possibilities to change the properties of the layer, which can be achieved on the nanometer scale by SPM.^{7,9,14,15}

In contrast to chemisorption, physisorption is not very suitable for making “permanent” architectures. Nevertheless, these

physisorbed adlayers are model systems to investigate the interplay between molecular structure and the formation of ordered assemblies in two dimensions.¹⁶

STM is one of the preferred techniques to investigate the ordering and properties of these self-assembled layers, in general monolayers, both under ultrahigh vacuum conditions as well as at the liquid/solid or air/solid interface. In STM, a metallic tip is brought very close to a conductive substrate and by applying a voltage between both conductive media, a tunneling current through a classically impenetrable barrier results between the two electrodes. The direction of the tunneling depends on the bias polarity. The exponential distance dependence of the tunneling current leads to excellent control of the distance between the probe and the surface, and very high resolution (atomic) on atomically flat conductive substrates can be achieved. For imaging purposes, the tip and substrate are scanned precisely relative to one another and the current is accurately monitored as a function of the lateral position. The contrast in STM images reflects both topography and electronic effects. In the constant height mode, the absolute vertical position of the probe remains constant during raster scanning and the tunneling current is plotted as a function of the lateral position.

Successful monolayer formation and STM imaging require balanced molecule–substrate interactions: a too strong interaction immobilizes the molecules and impedes self-assembly into ordered 2D layers. A too weak adsorbate–substrate interaction leads to a too high mobility, and high-resolution STM imaging becomes impossible.

The organic liquid/solid interface provides a particularly interesting environment to carry out the self-assembly experi-

* To whom correspondence should be addressed. E-mail: Frans.DeSchryver@chem.kuleuven.ac.be. E-mail: Steven.DeFeyter@chem.kuleuven.ac.be. Fax: +32 16 327989.

ments and their investigation by scanning tunneling microscopy.^{17,18} Compared to sample preparation and measuring under UHV conditions, the liquid/solid interface has a number of advantages: (1) The experimental approach is straightforward and does not require a complicated or as expensive infrastructure. (2) Though the UHV environment provides excellent control leading to unprecedented high resolution,^{19–23} not all species can be adapted to UHV, such as those with relatively low thermal stability or big size. The demands set on the properties (size and function) of the molecules under investigation at the liquid/solid interface are more relaxed. (3) The choice of solvent can be tuned in function of the particular solute and/or substrate. Typically, the solvent has a low vapor pressure, is nonconductive (electrochemically inert), and shows a lower affinity for the substrate than the solute. (4) The dynamic exchange of molecules adsorbed on the surface and in the liquid phase promotes repair of defects in the self-assembled layers. As a result, the liquid/solid interface approach in combination with STM imaging is becoming increasingly popular to induce and investigate self-assembly on surfaces.^{24–27} Additional control of the monolayer formation can be achieved under potential control in aqueous solutions. Under electrochemical conditions, adsorbate–substrate interactions can be modulated by the surface charge density. Electrochemical environments offer therefore additional possibilities to control surface dynamics and monolayer structure via the surface charge and to image those structures by means of electrochemical scanning tunneling microscopy: EC–STM.^{28–31}

In this contribution, we give an overview of our latest efforts related to the study of monolayer formation and their properties at the organic liquid/solid interface with a focus on 1) structure and control of monolayer formation 2) reactivity 3) and spectroscopy.

Hydrogen Bonding and Control of Monolayer Structure...

Hydrogen bonding has been amply explored for self-assembly purposes in solution and in three-dimensional (3D) crystals.^{32,33} Although hydrogen bonding has been exploited for self-assembly at surfaces too, including the liquid/solid interface,^{34–40} the control of the supramolecular patterns of a given hydrogen bonding synthon to form a variety of different 2D supramolecular structures has not received as much attention. Let's consider the case of the isophthalic acid derivatives. The main feature of an isophthalic acid is the presence of two carboxylic acid groups in the 1,3 position of the phenyl ring. These carboxylic acid groups tend to dimerize, so hydrogen bonding is expected to contribute significantly to the molecular ordering. The two carboxylic acid groups are in the meta position, so the angle between both is 120°. Depending on the nature of the alkyl chains, the supramolecular hydrogen bonding motif can be tuned.⁴¹ Two extreme cases are presented in Figure 1. Isophthalic acid derivatives with a linear alkyl chain in the 5 position, such as **1**, self-assemble into a 2D crystal at the liquid/solid interface as revealed by STM (Figure 1A). The aromatic isophthalic acid (ISA) groups show up bright, whereas the alkyl chains are darker. The ISA groups are arranged in a double row adopting a distorted “zig/zag” pattern. The distance between equivalent isophthalic acid rows measured along the alkyl chains is 36 ± 2 Å. The alkyl chains are fully extended, interdigitated, closely packed, and almost perpendicular to the lamella axis. Both rows of adjacent **1** molecules are hardly shifted with respect to each other, and the intermolecular distance between ISA moieties along a row measures only 9.4 ± 0.2 Å. Despite the directional nature of hydrogen bonding, optimal hydrogen

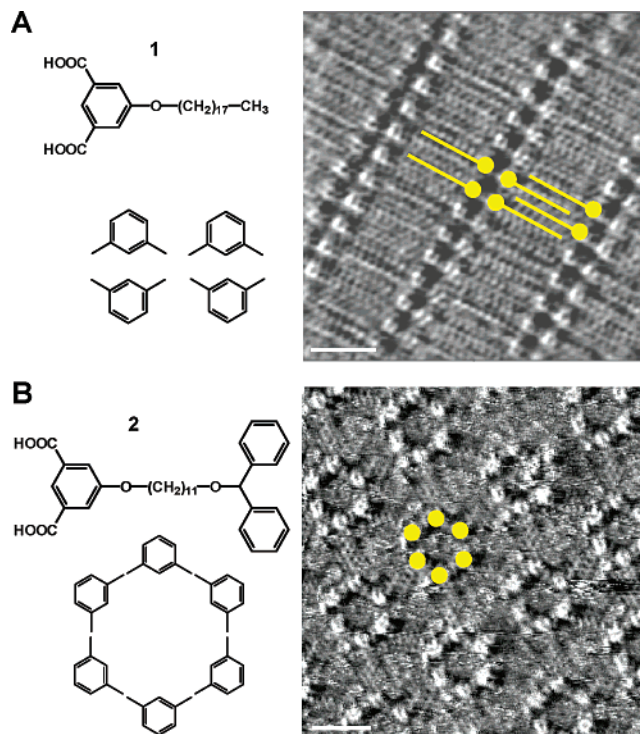


Figure 1. Chemical structures, representative STM image and schematic motif of isophthalic acid derivatives physisorbed at (A) the 1-phenyloctane/graphite interface for **1** and (B) the 1-octanol/graphite interface for **2**. Results are identical for **1** at the 1-octanol/graphite interface, except for the fact that in some areas of the monolayer, 1-octanol solvent molecules are coadsorbed (not shown). The scale bar in the STM images (lower left) represents 2 nm. Some simple stick models are indicated in the STM images: the circle and the sticks represent the aromatic ISA groups and alkyl chains, respectively. The schematic motifs indicate the ordering of the ISA cores and the direction of the carboxylic acid groups.

bonding between ISA groups based upon the classical carboxylic acid dimer is not formed at the liquid/solid interface. The graphite (HOPG) surface has a pronounced influence on the ordering of the molecules as the alkyl chains are running parallel to one of the main graphite symmetry axes. In contrast, a new motif is formed when bulky benzhydryl groups are introduced at the end of a long alkyl chain (**2**). This molecule exclusively shows the formation of rosette structures, containing six molecules. The rosettes are by themselves organized in a hexagonal arrangement. The bright features are attributed to the location of the aromatic ISA groups, and close inspection indeed shows that every ring is composed of six bright spots, indicating stabilization by hydrogen bonding. The interior of these rosettes might be filled with mobile solvent molecules. The benzhydryl and the alkyl groups are not clearly visible in the STM image which we attribute to the mobility of the chains on the graphite surface caused by the lack of interchain van der Waals interactions and free volume. Changing the nature of the alkyl chain affects the hydrogen bonding motif formed.

Tuning the intermolecular interactions by tailoring the non-covalent interactions indeed leads to control of the self-assembly process. The hydrogen bonding motif itself can also be used to direct the ordering of the molecules. Of special interest are those molecules with “functional” moieties, such as conjugated oligomers. *p*-Phenylene vinylenes are such an important class. Three types of chiral *p*-phenylene vinylenes have been investigated (Figure 2), which differ in their hydrogen bond forming abilities.^{42–45} They all carry (*S*)-2-methyl butoxy groups along the backbone. In the first type, oligo-*p*-phenylene vinylenes,

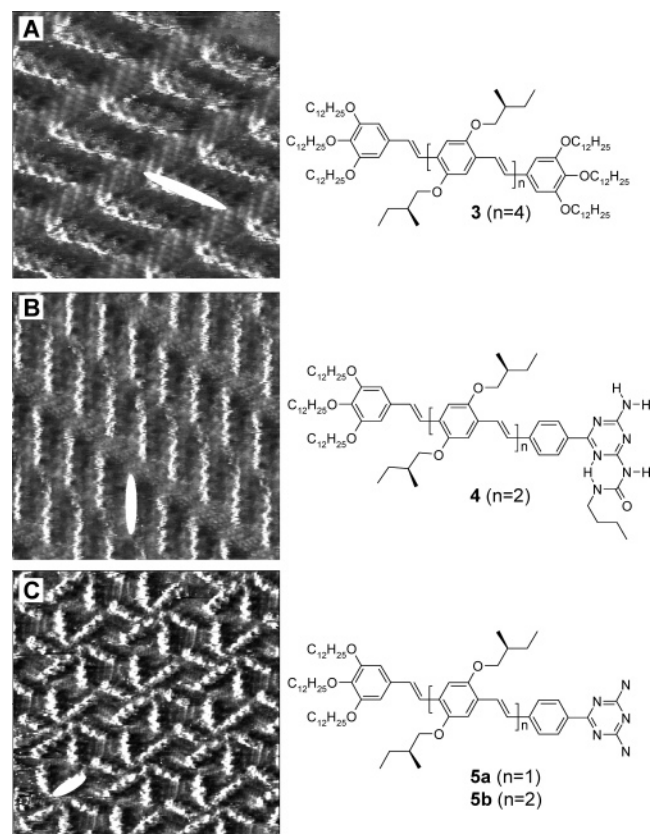


Figure 2. STM images and chemical structures of (A) **3** ($n = 4$) at the 1,2,4-trichlorobenzene/graphite interface (image size: $10.7 \times 10.7 \text{ nm}^2$); (B) **4** ($n = 2$) at the 1,2,4-trichlorobenzene/graphite interface (image size: $12.1 \times 12.1 \text{ nm}^2$); and (C) **5a** ($n=2$) at the 1-phenyloctane/graphite interface (image size: $18.4 \times 18.4 \text{ nm}^2$). Hydrogen bonding has a strong effect on the supramolecular architecture. The white ovals indicate a conjugated backbone.

which are at both termini functionalized with three dodecyl chains (**3**) (Figure 2A), self-assemble in highly organized 2D crystals on graphite by spontaneous self-assembly.⁴² They form stacks, and the bright features correspond to the conjugated backbones, of which one is indicated by a white oval. Alkyl chains are interdigitated.

In the second and the third type, the molecules are functionalized by hydrogen bonding groups such as ureido-*s*-triazine (type 2) (**4**) (Figure 2B) or 2,5-diamino-triazine groups (**5**) (type 3) (Figure 2C). The ureido-*s*-triazine derivatized oligo *p*-phenylene vinylenes show *linear dimerization* via self-complementary hydrogen bonding, as expected.⁴³ The molecules are indeed stacked in parallel, though not equidistant, rows. The fact that the conjugated backbones forming a dimer are slightly shifted is in line with the hydrogen bonding pattern formed. In contrast, the 2,5-diamino-triazine derivatized oligo *p*-phenylene vinylenes show *cyclic hexamer* formation.^{44,45} By functionalizing the oligomers, the ordering can be controlled. In none of the systems, intermolecular π - π stacking is achieved. π - π stacking parallel to the surface is essential when it comes to in plane directional charge transport, as required in for instance field-effect transistors.⁴⁶ To achieve π - π stacking interactions of the molecules on the surface, another design is mandatory.

...Also in Multicomponent Systems...

Such enforced overlap can be realized by hydrogen bonding interactions directed perpendicular to the long axis of the conjugated oligomers. We used the latter approach to generate

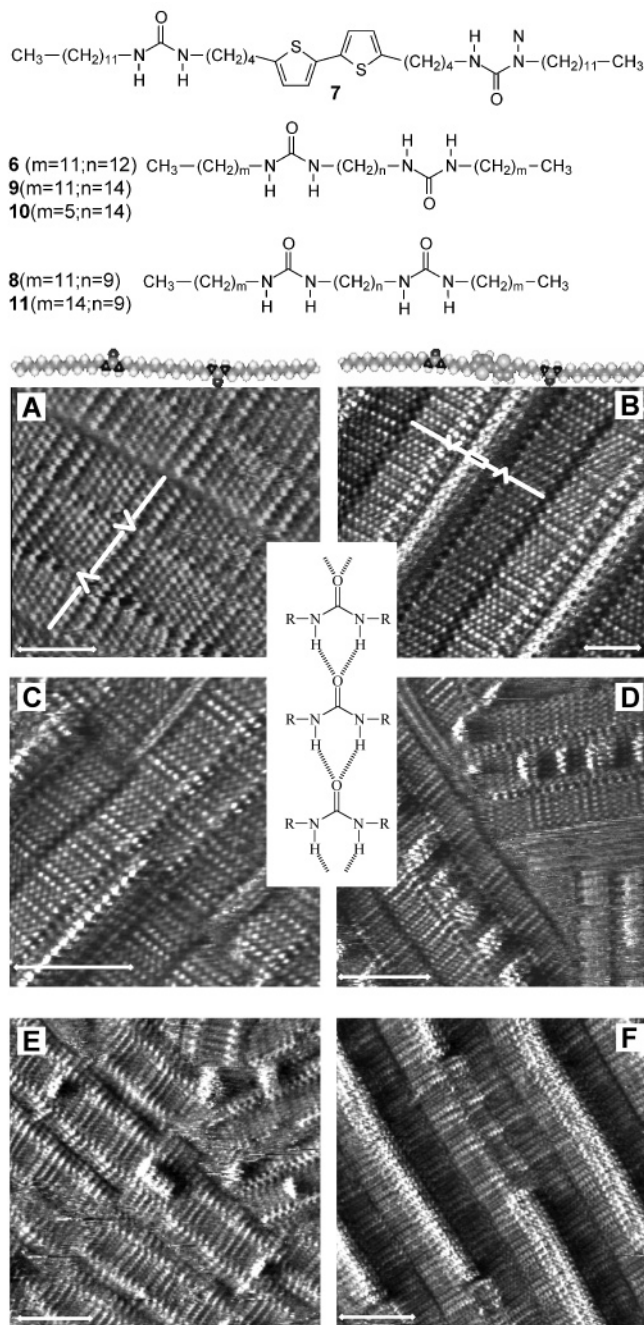


Figure 3. STM images at the 1-octanol/graphite interface of (A) **6** and (B) **7** and mixtures of (C) **7** and **8**: complete phase separation; (D) **7** and **9**: optimal mixing; (E) **7** and **10**: in addition to clusters, isolated molecules of **7** are observed; (F) **7** and **11**: complete phase separation. **7** can be recognized by the as bright appearing bithiophene units in the center of a row. The scale bar indicates 4 nm.

closely packed 2D arrays of thiophenes at the liquid/solid interface by means of introducing urea groups in the alkyl substituents of the thiophenes.⁴⁷ Alkyl-substituted bis-urea derivatives assemble efficiently at the liquid/solid interface.^{48–50} These molecules physisorb on the graphite substrate with their long molecular axis parallel to the substrate while forming extended lamellae. The dominating intermolecular interaction is the formation of hydrogen bonds between the urea groups. Within a lamella, each molecule is stabilized by eight hydrogen bonds, which determines the intermolecular distance of 0.46 nm. Figure 3A shows an STM image of **6**.^{49b} We have taken advantage of the well-defined intermolecular hydrogen bonding interactions to induce stacking of oligothiophenes. Figure 3B

shows a typical STM image of a densely packed monolayer of **7** adsorbed from a solution in 1-octanol onto the graphite substrate.⁴⁷ The molecules are arranged in lamellae. In the center of a lamella, two rows of bright spots can be discerned corresponding to the location of the two thiophene rings. The intermolecular distance is 0.46 nm, indicating hydrogen bonding. In addition, molecular modeling, corroborated by molecular mechanics and molecular dynamics calculations, reveal that the thiophene rings are not lying flat on the substrate but make an angle with the substrate surface and can interact with each other by their aromatic planes.⁴⁷ In addition, the formation of well-defined oligothiophene assemblies was targeted, revealing that control of the phase behavior of structurally related compounds can be achieved where the main mode of intermolecular interaction is hydrogen bonding. Therefore, **7** was mixed with analogous compounds, in which the bithiophene group was replaced by an alkyl spacer.⁵⁰

The distance between the two urea groups of **7** corresponds to an alkyl chain containing 14 carbon atoms, as in compound **9**. The alkyl chain linking the two urea moieties is called the spacer. Mixing of **7** with compounds having dodecyl terminal groups but an alkyl spacer ranging from 6 to 16 carbon atoms shows that optimal mixing is obtained with **9**, whereas complete phase separation is obtained for **8**. The images of the mixed systems were analyzed in terms of the size of the “aggregates” of **7** formed: monomers, dimers, trimers, tetramers, pentamers, and assemblies which contain more than 5 molecules of **7**. The monomer content increases in going from 6 carbon atoms in the spacer to 14 carbon atoms and decreases with increasing spacer length. The opposite trend is found for the large assemblies of **7**. If the spacer length differs by more than five carbon atoms, phase separation occurs: only “infinite” stacks of **7** and the other bisurea derivative are observed. If the difference in spacer length is smaller than 5 carbon atoms, in addition to the formation of large assemblies of **7**, a substantial contribution of monomers and smaller size assemblies is present. More important than the difference in molecular size seems to be the fact that for those compounds with an alkyl spacer length different from 14 carbon atoms the urea groups cannot form ideal intermolecular hydrogen bonding. This has been confirmed by mixing **7** with a molecule **10** having a tetradecyl spacer but with terminal hexyl chains instead of dodecyl chains. Though this molecule is much shorter than **6**, **7** and **10** mix very well as their identical spacer length still allows hydrogen bonding along a stack. The importance of hydrogen bonding as the most important interaction in this system is finally confirmed by mixing **7** with bisurea derivatives which are identical in length as **7** but which have the urea groups located at different positions along the molecular axis, such as **11**. Despite their identical dimensions the molecules completely phase separate.

As demonstrated phase separation is promoted by an increase in the difference in molecular length, whereas randomly intermixing is optimal when the length of both components is identical. In addition, the presence and the location of the hydrogen bonding units in the molecules play an important role. Hydrogen bonding can counteract the effect of the difference in molecular length on the 2D phase behavior. Differences in the electronic properties related to the size of the **7** aggregates have been probed by scanning tunneling spectroscopy, revealing that size indeed matters.⁴⁸

Although it is not possible to control the size of the aggregates, by paying attention to the intermolecular interactions, the phase behavior leading to optimal mixing or phase separation can be influenced to a large extent.

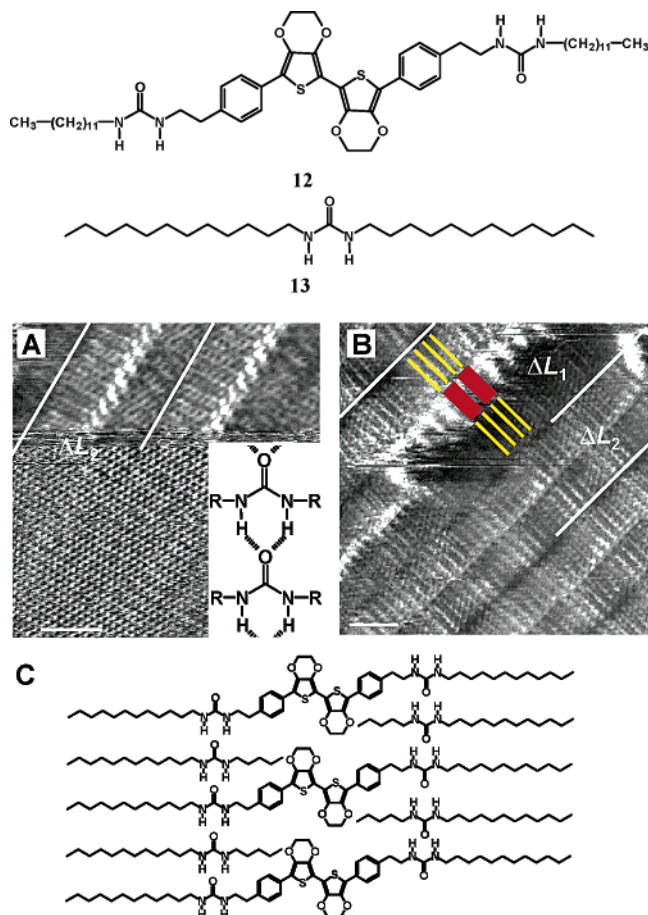


Figure 4. STM images of monolayers of (A) **13** adsorbed at the 1-octanol/graphite interface. The urea groups appear bright. The bias voltage was suddenly decreased during scanning, revealing the graphite substrate underneath the monolayer. ΔL_2 is the lamella width. The inset represents the hydrogen bonding motive between urea groups. (B) STM images of monolayers of a **12/13** mixture adsorbed at the 1-octanol/graphite interface. Solid arrows point to urea groups of **12**. ΔL_1 is the lamella width of **12**. ΔL_2 is the lamella width of **13**. The red boxes correspond to the conjugated units. The yellow lines are alkyl chains. The scale bar measures two nm. C) Simplified model illustrating the co-deposition pattern of **12** and **13**. For clarity, the dodecyl groups of **13** pointing to the center of the lamella are only shown in part. Due to space limitations, those dodecyl groups are not fully extended and part of the alkyl chain is expected to point to the solution. Note that, in reality, the conjugated units groups do not lie flat on the substrate.

The size of the bithiophene units and the intermolecular distance, dominated by the intermolecular hydrogen bonding between the urea groups, are quite compatible. The question rises, what happens when there is not a perfect match? This incompatibility clearly showed up while investigating the 2D self-assembly of **12** on the basal plane of HOPG.⁵¹ To our surprise, no 2D ordering of **12** was observed by STM, regardless of the solvent used. This lack in ordering was attributed to the bulky nature of the ethylenedioxy thiophene group, which prohibits an optimal shape and functionality complementarity. As an alternative approach to promote adsorption and stable monolayer formation, mixed solutions of **12** and mono-urea derivative **13** were investigated. The idea was that coadsorption of **2** might “dilute” the system and relieve the steric interactions. Compound **13** forms monolayers by itself, and Figure 4A shows some typical features. Domains consist of parallel lamellae. The urea groups show up in the images often as the brighter features and are aligned in rows. The alkyl chains are oriented perpendicular to the row of urea groups and run parallel with a

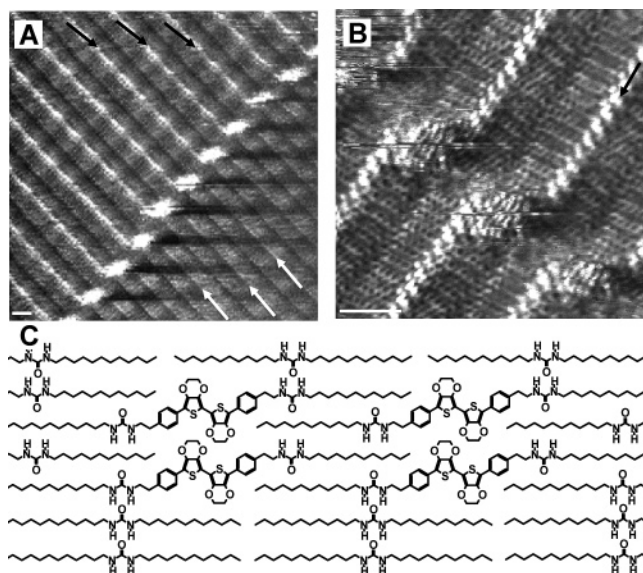


Figure 5. (A,B) STM images of monolayers of a **12/13** mixture adsorbed at the 1-octanol/graphite interface. The scale bar represents two nm. The black and white small arrows indicate rows of urea groups. (C) Tentative model illustrating the interactions leading to the formation of the clusters of **12** at the domain boundary. Due to interdigitation of the alkyl chains, adjacent **12** molecules do most likely not interact via hydrogen bonding.

major symmetry axis of graphite. The lamella width measures $3.5 \text{ nm} \pm 0.1 \text{ nm}$, which is in agreement with an extended and flattened conformation of the molecules. The intermolecular distance equals again 0.46 nm . When a mixture was applied, monolayer formation was observed (Figure 4B). In addition to the characteristic features of **13**, individual bright structures are observed, of which the width corresponds to the size of the conjugated segment. The average intermolecular distance between two adjacent bright structures equals $0.84 \text{ nm} \pm 0.05 \text{ nm}$, which is much larger than expected based upon the “normal” intermolecular distance of urea derivatives (0.46 nm). In addition, the number of visible alkyl chains is twice the number of bright structures, which suggests that within a lamella an alternating sequence of **12** and **13** is formed, releasing the strain otherwise imposed by adjacent molecules of **12**.

At domain boundaries between two domains composed of **13**, which are shifted with respect to each other by about half a molecular length, sometimes bright structures reflecting the presence of conjugated cores were observed. Such bright spots correspond only to a few **12** molecules at most and during imaging, the size of these nanoassemblies was not observed to change (Figure 5). The formation of these kinds of isolated clusters with a very small size distribution is a unique phenomenon in two dimensions. The origin of the limited size of these nanoassemblies is interpreted as the result of the balance between stabilizing (hydrogen bonding) and destabilizing (“steric” hindrance) interactions, as shown in the models.

...And in Combination with Fluorophobic/Fluorophilic Interactions

Hydrogen bonding is one of the possible noncovalent interactions to control nanophase behavior but not the only one. To gain insight into the interplay between hydrogen-bond formation and fluorophilic/fluorophobic interactions on the 2D phase behavior, we have investigated the self-assembly of semifluorinated alkylated isophthalic acid derivatives which differ in the length of the alkyl chains and the ratio of the length

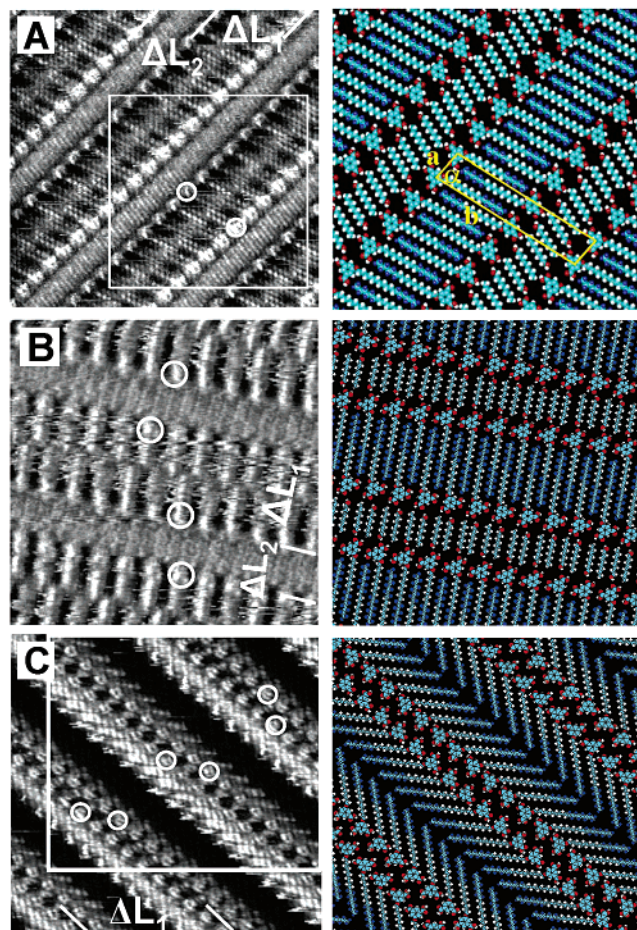
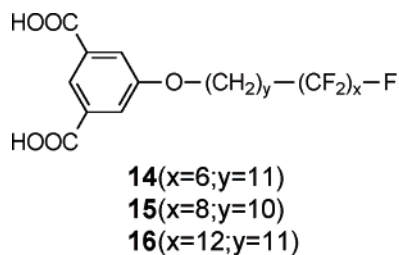


Figure 6. STM images and corresponding model at the 1-octanol/graphite interface of a monolayer of (A) **14** (image size: $13.1 \times 13.1 \text{ nm}^2$); (B) **15** (image size: $10.1 \times 10.1 \text{ nm}^2$); and (C) **15**, (image size: $10.6 \times 10.6 \text{ nm}^2$). Alternating dark and bright rows can be clearly distinguished. The dark row corresponds to the fluorinated part of the molecule, while the bright row corresponds to the nonfluorinated part plus the isophthalic acid group (indicated by white circles). ΔL_1 indicates a lamella of FxHy-ISA while ΔL_2 indicates a solvent lamella.

of the fluorinated segment versus the nonfluorinated segment.^{52,53} Alkylated isophthalic acid derivatives typically form a pattern where the alkyl chains are fully interdigitated. It was expected that fluorophilic/fluorophobic interactions would affect the packing of the molecules.

Typical monolayer STM images of **14** (F6H11-ISA) and **15** (F8H10-ISA) are shown in Figure 6, the result of the self-assembly process at the 1-octanol/graphite interface. The perfluorinated segments can clearly be distinguished by their characteristic dark contrast. The alkyl chains are fully interdigitated and each perfluorinated segment has two nonfluorinated segments as nearest neighbors. This supramolecular organization is very similar to the behavior of nonfluorinated 5-alkoxy-isophthalic acid derivatives. In addition, a row of coadsorbed 1-octanol molecules separates FxHy-ISA lamellae. Co-deposition of 1-alcohol molecules is observed for a sub-

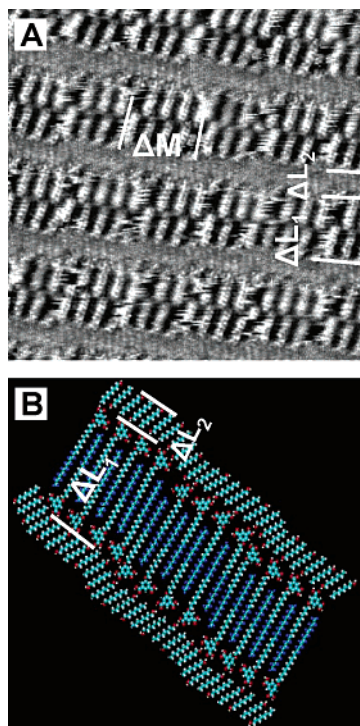


Figure 7. (A) STM image of a monolayer of **16** physisorbed at the 1-octanol/graphite interface. The molecules group into units of about 8 molecules. One unit is indicated by ΔM . ΔL_1 indicates a lamella of **16**, whereas ΔL_2 indicates a solvent lamella (image size: 20.8×20.8 nm²). (B) Molecular model of monolayer.

stantial number of 5-alkoxy-isophthalic acid derivatives.²⁷ It came as a surprise that the monolayer formation was not affected and that no nanophase separation occurred, despite the presence of the fluorinated segments. However, in the early stages of monolayer formation of **15** (F8H10–ISA), another packing was observed. The molecules are arranged in a bilayer type structure where the fluorinated part of the alkyl chains can clearly be distinguished as a black band. Individual perfluorinated alkyl chains cannot be distinguished. Image analysis shows that the alkyl chains are not interdigitated but that they make an angle with the growth direction of the lamellae. In time, within an imaging session, the monolayer structure changes into an interdigitated lamellar one, with co-deposition of solvent molecules. The dynamic formation of this pattern is interpreted as the result of a compromise between opposing interactions arising from the chemical structure of the molecules, where the interaction between the perfluorinated and nonfluorinated segments tend to induce nanophase separation, whereas the hydrogen bonding network of the isophthalic acid groups and coadsorbed solvent molecules tend to induce an interdigitated lamellar structure.

To have a larger impact on the phase behavior, the self-assembly of an alkylated isophthalic acid derivative with yet a longer fluorinated part was targeted **16** (F12H11–ISA), expecting that increasing the length of the fluorinated part would disturb the delicate balance of the intermolecular interactions, finally giving rise to nanophase separation. Indeed, a change was observed but not the expected one (Figure 7). The molecules appear in small units consisting of about eight molecules of which the alkyl chains are interdigitated and solvent molecules are coadsorbed. Each unit is shifted by 4.2 ± 0.4 Å with respect to the preceding unit. The incompatibility induced by the fluorinated chains is expressed at two levels. First, the molecules group into units, until the lattice cannot tolerate the incompat-

ibility induced by the F12 groups. It should be stressed that, at the interface between two units, the intermolecular interactions are optimized, resulting in close contacts between the perfluorinated–perfluorinated and the nonfluorinated–nonfluorinated parts of the adjacent molecules. Second, the increased mobility of the alkyl chains, often the alkyl chains lack any contrast or appear with streaky features parallel to the scan direction (left to right), is a result and a clear demonstration of the incompatibility between the perfluorinated segments and the nonfluorinated ones.

The strong incompatibility of perfluorinated and nonfluorinated segments and the weak perfluorinated segments–substrate interactions tend to induce nanosegregation in the monolayer. At the same time, the interaction of nonfluorinated segments with the graphite surface in addition to the hydrogen-bonding network formed between the isophthalic acid groups and solvent molecules tend to induce interdigitation. Hence, the observed packing patterns of the semifluorinated isophthalic acid derivatives at the liquid/solid interface are a delicate compromise between these often opposing interactions within the monolayer.

So, Do Not Forget about the Role of Solvent!

Indeed, as we have shown above the solvent plays an important but often underestimated role in the 2D ordering of the molecules at the liquid/solid interface. Another example is the solvent dependent self-assembly of a monodendron **17** at the liquid/solid interface.⁵⁴ At the 1-octanol/graphite interface, tetramers are formed which appear distorted, and from row to row, the tetramers are tilted with respect to each other (Figure 8A–C). Tentatively, each bright spot can be assigned to the location of a phenyl ring. The gray-like striped features are the alkyl chains. A unit cell is indicated in Figure 8A, which contains eight molecules. The distance between two adjacent alkyl chains is approximately 0.46 nm. The formation of tetramers might be due to hydrogen bond formation via the carboxylic group of one monodendron and the hydroxyl group of another monodendron. The phenyl rings are surrounded by alkyl chains. The distance between the tetramers along the vector **a** measures 3.80 ± 0.06 nm. The alkyl chains between the tetramers along this direction are most likely directed to the solution.

At the 1-phenyloctane/graphite interface, also tetramers are formed (Figure 8D–F). The alkyl chains are interdigitated and separated by approximately 0.46 nm and can be divided into two subsets, depending on their contrast. Those two subsets are oriented perpendicular to each other. From every monodendron, two alkyl chains are oriented almost perpendicular to the unit cell vector **a**, and those alkyl chains are oriented along one of the main symmetry axes of graphite. The third alkyl chain which appears with a higher contrast in the images is oriented along the unit cell vector **a**. The difference in contrast between the alkyl chains can be attributed to their different orientation with respect to the graphite lattice. Between two tetramers are four of the latter type of alkyl chains. As a result, the distance between two tetramers along unit cell vector **a** (4.69 ± 0.07 nm) is longer than for the pattern at the 1-octanol interface. In the direction perpendicular to the unit cell vector **a**, there is an excess of two alkyl chains for every tetramer. Most likely, two solvent molecules of 1-phenyloctane are coadsorbed per tetramer unit in the monolayer as illustrated in Figure 8E. The bright spots indicated by yellow arrows in Figure 8E,F correspond to the phenyl groups of the coadsorbed solvent molecules. These phenyl rings often appear rather fuzzy which suggests some

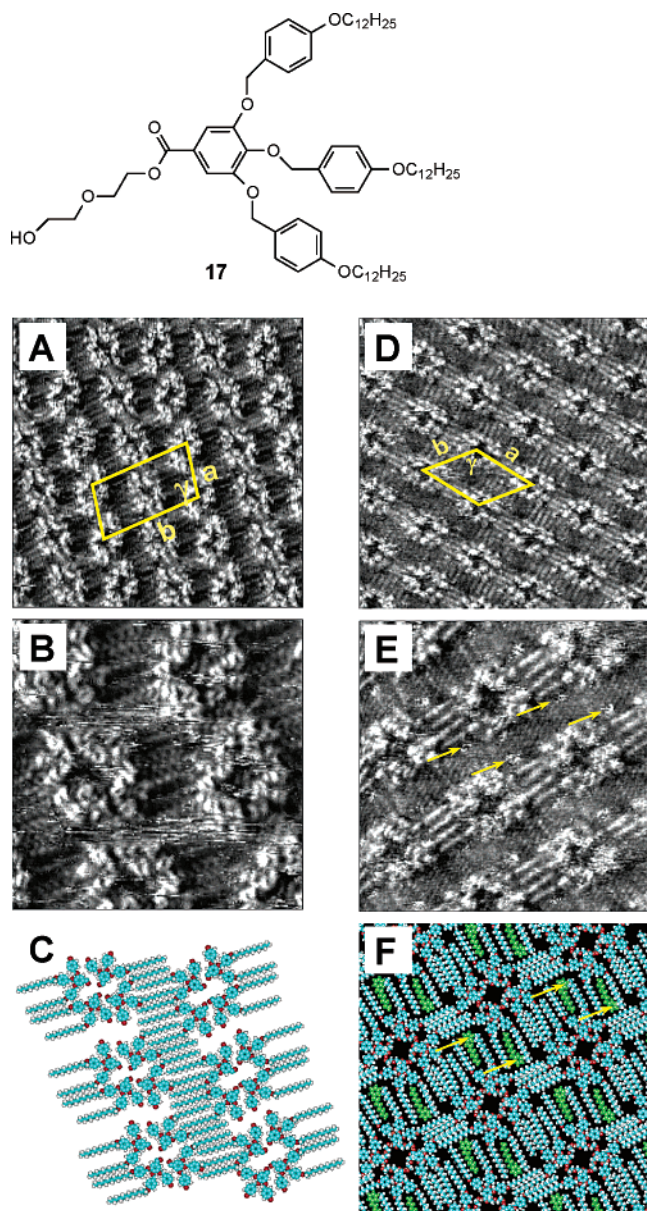


Figure 8. (A–C) STM images and model of monodendron **17** physisorbed at the 1-octanol/graphite interface. (A) Image size: 23.5 nm \times 23.5 nm². Unit cell is indicated in yellow. (B) Image size: 8.4 nm \times 8.4 nm². (C) Tentative molecular model. The alkyl chains along the unit cell vector *a*, and the hydroxyl group containing alkyl parts within the tetramers have been omitted. (D–F) STM images and model of monodendron **17** physisorbed at the 1-phenyloctane/graphite interface (D) Image size: 23 nm \times 23 nm². Unit cell is indicated in yellow. (E) Image size: 12.8 nm \times 12.8 nm. The location of the coadsorbed 1-phenyloctane solvent molecules is indicated in yellow. (F) Tentative molecular model. The 1-phenyloctane molecules are indicated in green and the location of the phenyl groups is indicated by yellow arrows.

motional freedom. This coadsorption leads to a densely packed 2D monolayer. It is remarkable that 1-phenyloctane is coadsorbed and immobilized. 1-Phenyloctane molecules do not show any tendency to form immobilized monolayers on graphite. After all, this is one of the reasons why 1-phenyloctane is used as solvent. Although 1-phenyloctane and 1-octanol molecules are comparable in size, only the former one is coadsorbed. This presents a clear example of the effect of solvent on the 2D ordering at the liquid/solid interface. At present, it's not clear why precisely 1-phenyloctane is coadsorbed and not 1-octanol. That's the subject of an ongoing study.

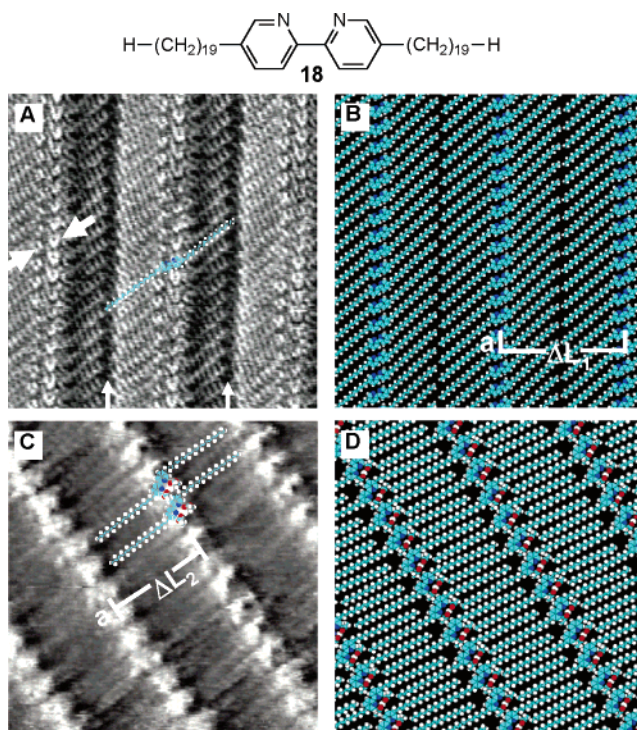


Figure 9. (A) STM image showing a monolayer of **18** physisorbed at the 1-phenyloctane/graphite interface. Big white arrows point to the aromatic rings forming the bipyridine moiety, and small white arrows define the lamella boundaries. One molecular model is superimposed for clarification. The different contrast of the alkyl chains on either side of the bipyridine cores is due to a scanning artifact. Image size: 9.1 \times 9.1 nm². (B) Molecular model. (C) STM image showing a monolayer of **18** physisorbed at the 1-phenyloctane/graphite interface after addition of Pd(OAc)₂ solution. Two molecular models are superimposed. Image size: 10.2 \times 10.2 nm². (D) Molecular model.

From Metal Complexation Reactions in Solution...

Metal complexation provides another interesting approach to control ordering. Upon applying a drop of **18** solution on the graphite surface (HOPG), a physisorbed monolayer is spontaneously formed at the 1-phenyloctane/graphite interface.^{55,56} Figure 9A shows an image of such a monolayer observed with STM. The image is submolecularly resolved, which enables us to identify the two aromatic rings forming the bipyridine moiety as well as the aliphatic chains. The lamella is defined by two black troughs, which are characteristic for terminal methyl groups. Based upon the contrast of the bipyridine moieties in the STM images, all of the molecules are equivalent along the lamella axis, and the molecules appear to be fully extended. The distance between two neighboring molecules within a lamella measured along the lamella axis (*a*) is 6.9 ± 0.3 Å, the lamella width ΔL equals 47.2 ± 1.6 Å. The packing parameters acquired from the STM image indicate that the bipyridine moieties are adsorbed parallel to the graphite plane, and there is no interdigitation of the aliphatic chains from neighboring lamella. After the successful imaging of the **18** monolayers at the 1-phenyloctane/graphite interface, a drop of Pd(OAc)₂ in 1-phenyloctane was applied to the same location of the initial drop. A spontaneous change of the monolayer packing pattern was observed (Figure 9C). The distance between two successive bright structures measured along the lamella axis (*a*) is 9.4 ± 0.1 Å, which is significantly larger than the distance of 6.9 ± 0.3 Å between bipyridine moieties before the addition of Pd(OAc)₂. A change in the packing pattern of the aliphatic chains is also evident; the alkyl chains are interdigitated. The distance between the neighboring molecules increases to 9.4 Å

in order to accommodate the $\text{Pd}(\text{OAc})_2$ between the bipyridine moieties, causing the aliphatic chains to interdigitate and reduce the free space in the monolayer. The orientation of the aliphatic chains with respect to the lamella axis changes from $49 \pm 2^\circ$ to $87 \pm 2^\circ$ after addition of $\text{Pd}(\text{OAc})_2$. The contrast arising from the complexed molecules suggests that $\text{Pd}(\text{OAc})_2$ is adsorbed on the graphite surface between the **18** molecules, where the palladium atom is on the graphite surface while the two acetate ligands are pointing toward the supernatant solution. The long-term goal of these experiments is to form stable templates, and then the use of such templates to assemble other molecules or nanostructures in the third-dimension. The stability of such templates in air is therefore a requisite and has been demonstrated.

Most likely, the formation of the complexed layer involves desorption of the noncomplexed molecules and readsorption of the complexed ones driven by changes in the concentration gradient of complexed and noncomplexed molecules in the solution on top of the substrate.

...To Polymerization Reactions at the Surfaces

Therefore, one can hardly claim that these functional molecules have reacted on the surface. However, certain reactions, such as topochemical polymerization reactions, are expected only to occur on the surface itself. A critical aspect in these kinds of reactions is the ordering of the monomers, both with respect to the distance and the orientation. Based upon the crystal structures of numerous diacetylene monomers and polymerized diacetylenes, maximal reactivity is expected when the stacking distance between two adjacent diacetylene moieties and the angle between the stacking axis and the diacetylene unit are $\sim 5 \text{ \AA}$ and $\sim 45^\circ$,⁵⁷ respectively. Some time ago, we demonstrated the possibility to induce a light-driven polymerization reaction at the liquid/solid interface.⁵⁸ Stimulated by a recent report of Aono et al.,⁵⁹ also tip-induced polymerization was targeted, both for an isophthalic acid derivative (**19**), containing one diacetylene unit, and a terephthalic acid derivative, containing two diacetylene chains (**20**), which has been designed and synthesized for the purpose of forming 2D linked nanostructures.⁶⁰ In a film of **19**, formed by transferring molecules at the water/air interface in an LB-trough by the horizontal lifting method to graphite, molecules form close-packed and well ordered lamella structures, and individual molecules are clearly resolved with molecular resolution (Figure 10A). In this case, the experiments were carried out at the air/graphite interface to stabilize the monolayers formed. The samples could be stored for several days. The lamella structure is characterized by the isophthalic acid (ISA) group and the diacetylene moiety of the molecules. The ISA groups appear bright and have a circular shape and the diacetylene moieties are brighter than the alkyl chains. The orientation of the diacetylene moieties alternates from lamella to lamella. After exposure of the film to UV irradiation, in addition to the monomer monolayer features observed, bright lines appeared which were never observed before irradiation (Figure 10B). The location of the bright lines coincides with the diacetylene moieties in nonilluminated films, and hence, this bright line is most likely a locally polymerized linear array of diacetylene moieties. In addition to the contrast change, the angle of the alkyl chains with respect to the lamella direction and the lamella width differ significantly between the polymerized array and the nonpolymerized array. The alkyl chains of the polydiacetylene make an angle of $102 \pm 3^\circ$ with the polydiacetylene backbone, whereas the alkyl chains are almost perpendicular to the diacetylene array ($87 \pm 2^\circ$) for

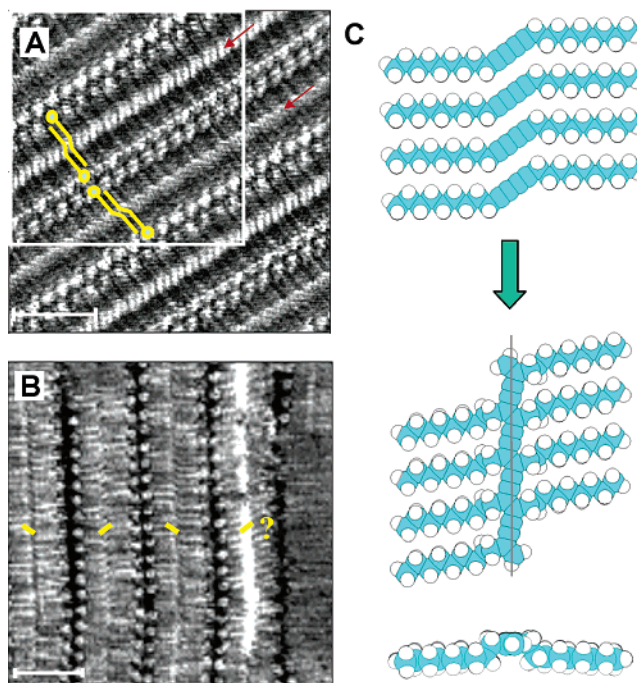
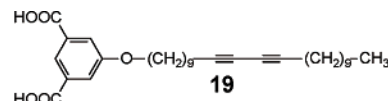


Figure 10. (A) STM image of monolayer of **19** on graphite deposited by the horizontal lifting method. Red arrows indicate the diacetylene moieties in the side chains. A few molecules are schematically drawn in yellow. (B) STM image of a monolayer of **19** after 30 min UV light irradiation. Orientation of the monomer diacetylene units prior to UV irradiation is indicated in yellow. (C) Tentative molecular model indicating that the polymer backbone is lifted from the substrate upon polymerization. The scale bar is 4 nm.

nonpolymerized lamellae. A similar observation was made for **20**. Interestingly, the interdigitation pattern of the alkyl chains of polymerized **20** of which the diacetylene units are not involved in the polymerization reaction is not affected.

As mentioned, polymerization has locally an effect on the orientation of the alkyl chains covalently bound to the polymer backbone. However, the direction of the reorientation is in line with the polymer chain propagation model as shown in Figure 10C in which the alkyl chains are parallel to the graphite surface but the innermost carbon atoms of the alkyl chains adjoining the polydiacetylene backbone and the polydiacetylene backbone itself are raised from the surface. By lifting up the polymer backbone, the alkyl chains can tilt and the model satisfies the experimental observations. Hence, the polymerized diacetylene backbone appears brighter in the STM image. Recently, Aono and co-workers identified the electronic structure of the polydiacetylene chains by scanning tunneling spectroscopy.⁶¹ Phase transitions were observed in these kinds of polymerized structures.⁶² **20** can form tightly packed molecularly well-ordered 2D monolayers. Due to the presence of two diacetylene units and the network formation by interdigitation of the alkyl chains, this compound is a potential candidate for the creation of 2D polymers. Figure 11A shows an STM image of a film of **20** prepared by the horizontal lifting method and irradiated for 30 min with UV light. The bright lines indicate the formation of three polymerized diacetylene rows. One of the possible reasons for the low polymerization yield is the substrate and/or the nonoptimal orientation of the diacetylene units. After the initial random polymerization induced by UV irradiation, a pulse

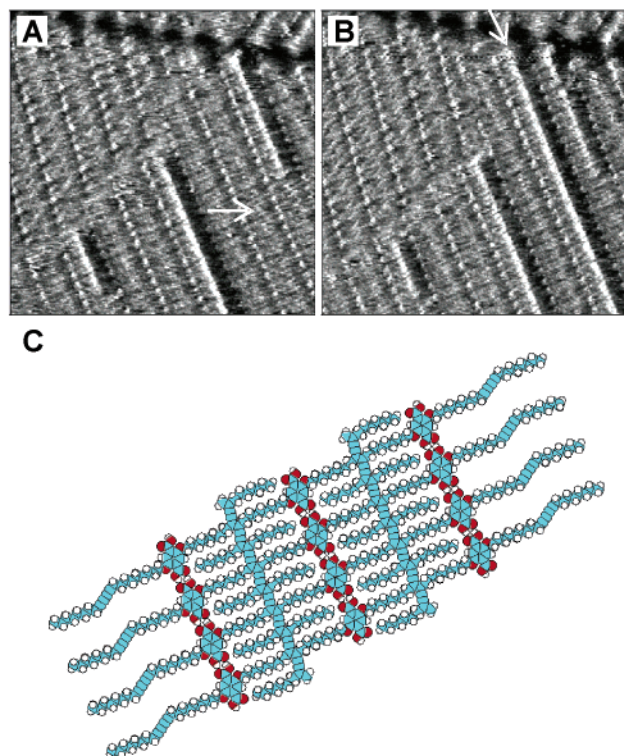
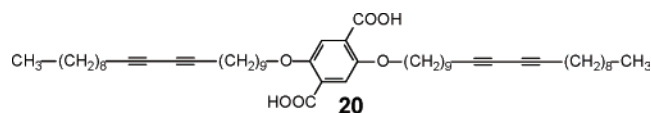


Figure 11. (A) STM image of a monolayer of **20** after 30 min of UV light irradiation. A pulse (height: -3.2 V; width: 500 ns) was applied at the position indicated with a white arrow. (B) STM image of the monolayer of **20** at the same area after application of a single pulse. The white arrow in the image indicates the polydiacetylene backbone created by pulsing. Scanning conditions for both A and B were identical. Image size: 27.1×27.1 nm². $I_{\text{set}} = 0.40$ nA, $V_{\text{bias}} = -0.40$ V. (C) Molecular model of a 2D nanostructure formed by the covalent connection of adjacent parallel polydiacetylene chains.

(height: -3.2 V, width: 500 ns) was applied in the middle of the image, indicated by the white arrow. A newly created polymerized diacetylene backbone is indicated by the white arrow in Figure 11B. The tip induced polydiacetylene chain is located next to a UV-light-induced polymer chain. The tip-induced polydiacetylene chain in Figure 11B propagates in both directions with respect to the location of the pulse. Figure 11C shows the schematic model of 2D connected 1D nanostructures of polydiacetylene. Clearly, adjacent rows of polydiacetylene chains are chemically connected, and form a 2D nanostructure.

A Twist of Chirality?

Since the late 1990s, the expression of molecular chirality at surfaces has received increasing attention. It is not the purpose to give an extensive overview of all of the work that has been reported on chirality at surfaces,⁶³ but this section is intended to give a flavor of the relation between self-assembly directed noncovalent interactions and chirality at surfaces from our laboratory. The manifestation of chirality in these essentially 2D systems can be used to control the orientation of the building blocks on a substrate. When 2D crystals are formed, they often appear to be chiral. This is often true, even for achiral molecules, but the 2D crystals of achiral molecules appear in an equal amount of mirror-image type domains in the absence of any discriminating influence. In almost all cases reported so far,

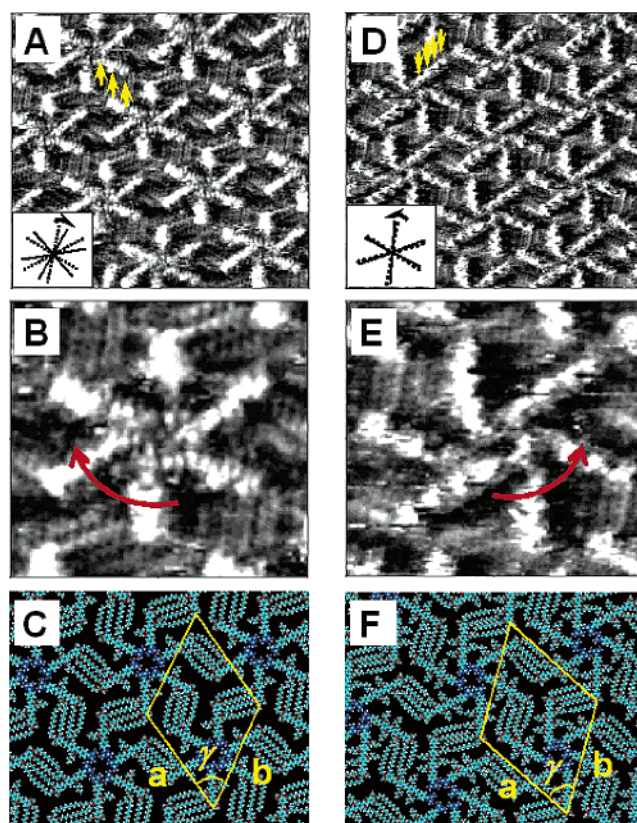


Figure 12. STM image of a monolayer of (A) **5a** (image size: 14.4×14.4 nm²) and (D) **5b** (image size: 18.4×18.4 nm²) physisorbed at the 1-phenyloctane/graphite interface. Yellow arrows point to intramolecularly resolved phenyl rings of the OPV backbone. Inset shows the propagation direction of rosette rows (solid line) and the main symmetry axes of graphite (dashed line). A unit cell is indicated in yellow. (B, E) A zoom of a **5a** and **5b** rosette. The red arrow indicates the “rotation direction” of the windmill. (C, F) Tentative model of the unit cell of **5a** and **5b**.

enantiopure molecules lead to the exclusive formation of one of the possible 2D mirror-type arrangements.^{64,65} For instance, in the case of **3** and **4**, molecular chirality is expressed by the orientation of the molecules within the domains: the π -conjugated backbone is oriented counterclockwise with respect to the normal on a lamella axis. Stereospecific molecule–substrate interactions result in a preferred adsorption of the enantiomer eliminating one of both mirror-image type (enantiomorphous) packings (i.e., unit cells).⁶⁶

Within these series of oligo-*p*-phenylene vinylene derivatives, compounds **5a** and **5b** take a special place. For both molecules, the arrangement of the molecules in individual rosettes is unidirectional but different for the two oligomers discussed (Figure 12). The **5a** rosettes appear exclusively to rotate clockwise (CW) (Figure 12A,B), whereas in **5b** rosettes, the molecules are exclusively arranged in a counterclockwise (CCW) fashion (Figure 12D,E). No rosettes of opposite chirality were found. Molecular chirality is transferred to the rosette structures which in turn form chiral 2D crystalline patterns. Intuitively, one would expect that the rosettes formed would show the same “rotation” direction, independent of the number of stereogenic centers or conjugated oligomer length. The difference in the virtual rotation direction of the **5a** and **5b** rosettes can be explained by balanced molecule–molecule and molecule–substrate interactions. Molecules tend on one hand to minimize the free surface area (favored by a CCW rotation), but in order to minimize steric interactions, a less dense packing might be more favorable (CW rotation). The final 2D pattern

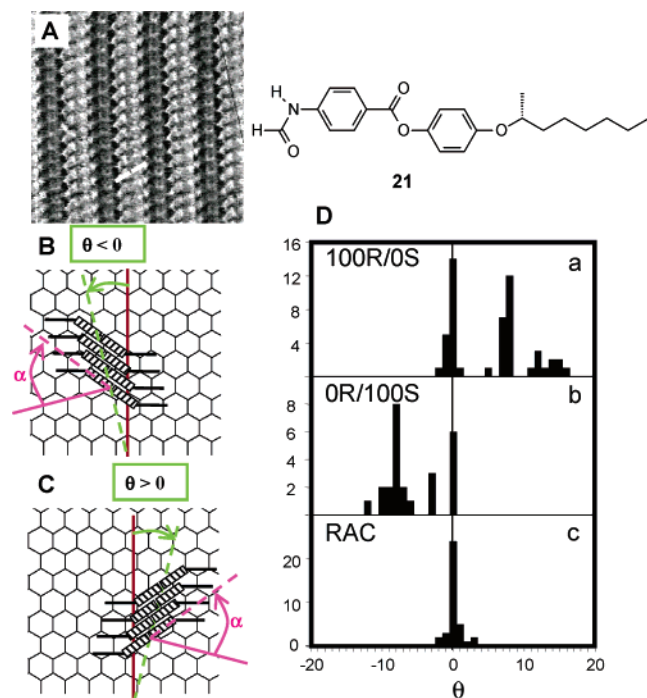


Figure 13. (A) STM image of (*R*)-**21** at the 1-heptanol/graphite interface. Image size: $11.0 \times 11.0 \text{ nm}^2$. Two phenyl benzoate groups are indicated by a white bar. (B, C) Schematic representations of the orientation of “dimers” of **21** on graphite. The reference axis of graphite is indicated in red. The dashed green line represents a lamella axis. θ : angle between the reference axis and the lamella axis. α : the angle between the normal on the lamella axis (solid purple line) and the orientation of the dimers (dashed purple line). (D) Histograms of the angle θ observed for physisorbed monolayers of (a) (*R*)-**21**, (b) (*S*)-**21**, and (c) (*rac*)-**21**.

is the result of a delicate balance between hydrogen bonding, van der Waals interactions between the alkyl chains and between the stereogenic centers and the substrate, and the free surface area, which is to a large extent affected by the ratio between the length of the conjugated backbone and the alkyl chains.

Chiral discrimination between mirror image stereoisomers can lead to the spontaneous spatial separation of a racemic mixture into the enantiomerically pure phases.⁶⁷ In 3D systems the formation of these so-called conglomerates is rather the exception than the rule: most racemic mixtures crystallize as racemates with the unit cell composed of an equal number of molecules with opposite handedness or as random solid solutions. Due to the confinement of the molecules in a plane and the interaction with the substrate, conglomerate formation becomes more likely. We compared the expression of chirality of two related molecules, **21** and **22**.^{68,69} The latter compound resembles **21**, except that the ester function linking the two aromatic rings is absent, a feature which is expected to affect significantly the intermolecular interactions.

In the STM images (Figure 13A), the phenyl benzoate moieties of **21** show up as the bright structures corresponding to high tunneling current through the aromatic groups. The alkyl chains are located between the rows of the phenyl benzoate groups, and sometimes their orientation can be discerned. The location and orientation of a number of phenyl benzoate groups are indicated by sticks. The molecules form chains which in turn form dimers. The X-ray data of their 3D crystals indicate hydrogen bonding interactions along the chains and between them through the formamide groups. The molecular chirality of the pure enantiomers of compound **21** is expressed at the 1-heptanol/solid interface at two different levels: (1) at the level

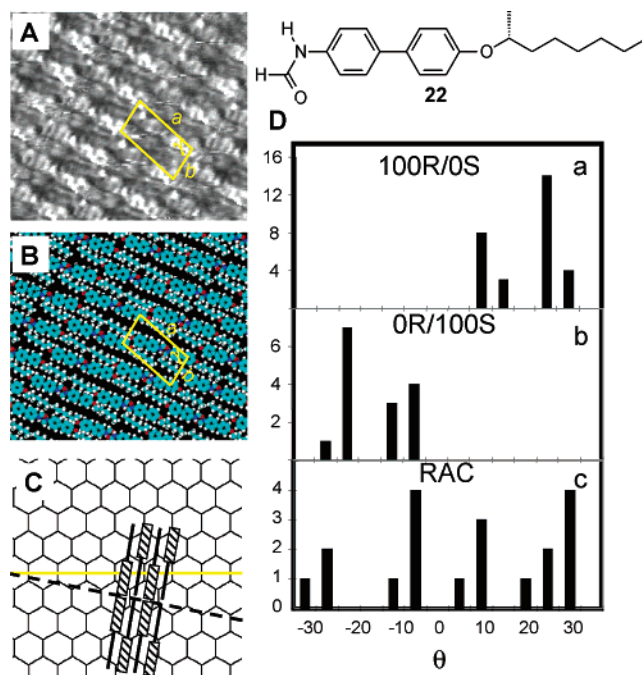


Figure 14. (A) STM image of (*rac*)-**22** at the 1-phenyloctane/graphite interface. Image size: $7.0 \times 7.0 \text{ nm}^2$. (B) A molecular model of a (*S*)-**22** type domain. (C) Schematic representation of the orientation of “dimers” of **22** on graphite, in case of a (*R*) enantiomer. The graphite symmetry axis is indicated in yellow. The dashed black line represents a lamella axis. (D) Histograms of the angle θ observed for physisorbed monolayers formed of (a) (*R*)-**22**, (b) (*S*)-**22**, and (c) (*rac*)-**22**.

of the monolayer structure as expressed by the orientation of the phenyl benzoate moieties (α) with respect to the lamella normal and (2) at the level of the orientation of the adlayer with respect to the underlying graphite lattice as expressed by the direction of the lamella axis of the monolayer with respect to the symmetry axes of graphite (θ) (Figure 13B,C). The latter correlation can be made because after imaging a monolayer each time the graphite lattice is recorded under identical experimental conditions except for lowering the bias voltage which allows imaging of the graphite surface underneath the monolayer. The histograms in Figure 13D represent the number of domains of which the lamella axis is rotated a given angle θ with respect to the graphite’s reference axis. Despite the considerable spread, in none of the three cases is the orientation of the lamella axis with respect to the substrate’s symmetry completely random. (*R*)-**21** has a strong tendency to form domains with $\theta > 0$ (Figure 13Da), whereas (*S*)-**21** forms preferentially domains with $\theta < 0$ (Figure 13Db). In addition, both enantiomers form a substantial fraction of domains for which the angle θ is close to zero (Figure 13Da–b). Similar results were obtained at the 1-phenyloctane/graphite interface.

In contrast to the enantiomers, the racemate forms *exclusively* domains with the angle θ_1 close to zero (Figure 13Dc). So, the patterns formed by the racemate are not a mere reflection of the adsorbate layers formed by the pure enantiomers. Therefore, no racemic conglomerate formation takes place.

For comparison, the 2D molecular packing of **22** was investigated. The brightest parts in the images can be assigned to the aromatic biphenyl groups (Figure 14A). The molecules appear in parallel rows with an alternating light and dark contrast. Taking into account the orientation of the monolayer with respect to the graphite symmetry, however, clear indications of chirality were found. The histograms in Figure 14D reflect the spread and frequency of the angle θ for (*R*)-**22**, (*S*)-**22**, and

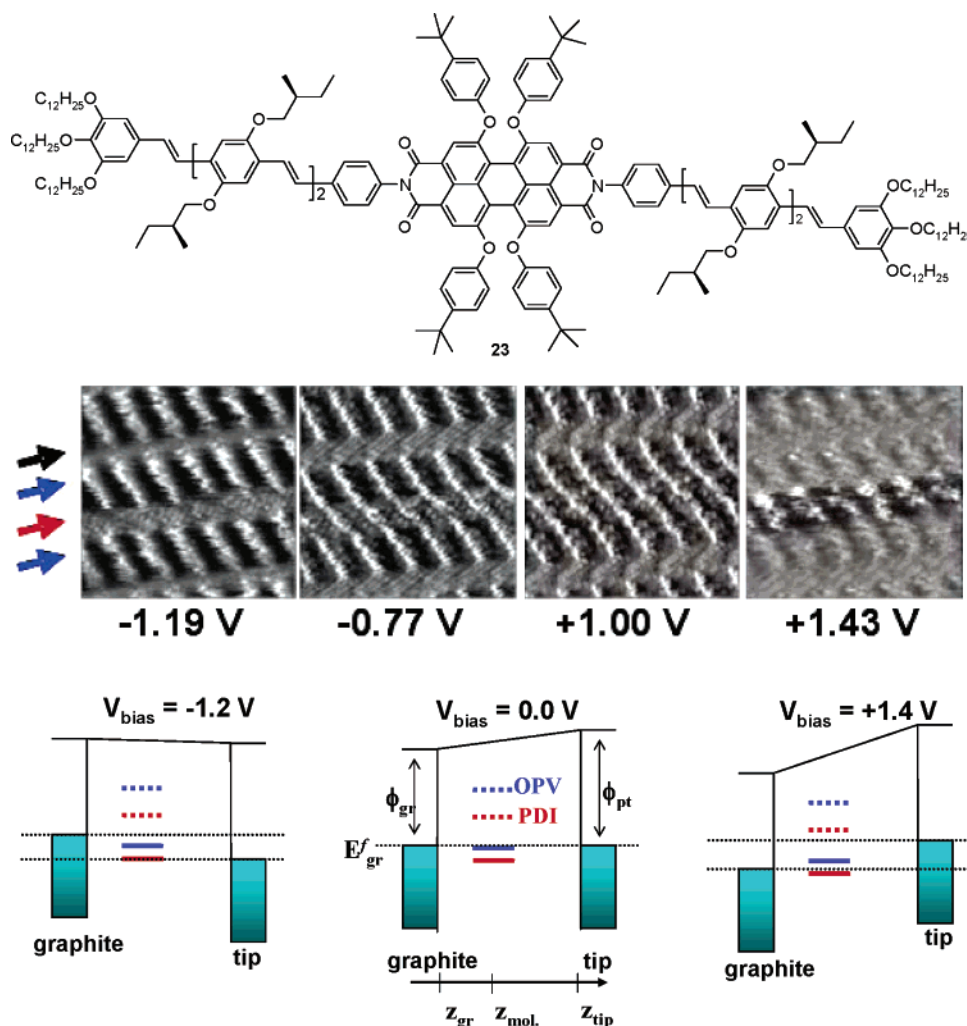


Figure 15. Top: Bias dependent imaging of **23** at the 1-phenyloctane/graphite interface. The applied sample bias is indicated below each image. Image size is $10.1 \times 10.1 \text{ nm}^2$. $I_{\text{set}} = 0.40 \text{ nA}$. Arrows outside the images refer to alkyl chains (black), OPV (blue), and PDI moieties (red). Bottom: Tentative energy level diagrams illustrating the relative position of the HOMO and LUMO levels of OPV (blue) and PDI (red) with respect to the graphite and Pt/Ir tip Fermi levels upon applying a bias on the sample. Left: negative sample bias. Right: positive sample bias. Fermi levels of graphite ($E_{\text{F,gr}}$) and STM tip ($E_{\text{F,t}}$) are indicated with black dotted lines.

the (*rac*)-**22** mixture. The total number of observations equals the number of different domains probed. For the (*R*) enantiomer as well as for the (*S*) enantiomer there is a bimodal distribution in the absolute values of the angle θ which peaks at $\sim 9^\circ$ and $\sim 24^\circ$. For (*R*)-**22**, this angle is always positive (Figure 14Da), whereas for (*S*)-**22**, θ is negative (Figure 14Db). The racemate (*rac*)-**22** gave equal contributions of positive as well as negative angles, similar to those absolute values found for the pure enantiomers (Figure 14Dc). This supports the conclusions drawn based upon the image contrast and the unit cells which strongly suggests that the biphenyl formamides undergo spontaneous resolution at the liquid/solid interface, in contrast to **21**. The question arises why, in case of **21** the racemate shows pseudoracemate formation, and the histogram in Figure 13Dc shows a monomodal distribution peaked at $\theta = 0$, whereas in case of **22** a racemic conglomerate is formed, and the histogram in Figure 14Dc reflects the contribution of both enantiomers. The major difference between both compounds is that in the case of **21**, both enantiomers have a phase with $\theta = 0$, a behavior not observed for **22**. As both enantiomers show a common $\theta = 0$ type ordering, bringing both enantiomers together in one domain (with $\theta = 0$) should be energetically allowed and entropically favored. In the absence of specific favorable interactions between both enantiomers of compound

22, forming a racemic compound will not be promoted. In case of **21**, the exclusive formation of $\theta = 0$ domains for the racemate suggests that there is a preferred interaction between both enantiomers, as opposed to the formation of homochiral domains.

Bright or Dark?

The way the molecules appear in STM images often depends on experimental parameters of which the bias voltage is a critical one. Indeed, STM is sensitive to the electronic properties of the adsorbates under investigation.⁷⁰ It was soon noticed that STM shows chemical sensitivity; certain functional groups (e.g., aromatic moieties, amines, and sulfides) are more conductive than others (e.g., alkyl chains). The latter are in turn more “transmissive” for the tunneling current than perfluorinated alkyl chains, as shown in previous paragraphs.⁷¹ Several theoretical approaches have been developed to explain the contrast of organic adsorbates in STM.⁷² Bias dependent imaging has been used to probe the electronic levels involved in the tunneling process,^{70c,73} but the system is unique for the following reasons: (1) it combines an electron donor (D = oligo-*p*-phenylene vinylene (OPV)) and electron acceptor part (A = perylene diimide (PDI)), covalently linked to each other and

(2) the donor and acceptor parts are relatively large and well-separated in space, allowing addressing them individually.⁷⁴

The compound forms well-ordered 2D patterns when physisorbed from 1-phenyloctane on HOPG at the liquid/solid interface, as measured by STM in the constant-height mode. The tunnel path through the aromatic core is tip-D-graphite or tip-A-graphite and not tip-D-A-D-graphite. Of course, the tunneling direction (tip-graphite or graphite-tip) depends on the bias polarity. Alkyl chains occupy the dark regions between the rows of bright rods. From the high-resolution images, it appears that the bright rods consist of three parts: the central part is attributed to the location of the PDI part, the outermost parts correspond to the OPV moieties.

At high negative voltages (-1.19 to -1.06 V), the OPV parts appear brighter compared to the central PDI moiety. By changing the bias voltage from negative to positive, the PDI part gradually becomes brighter (from -0.77 to $+0.80$ V). Upon further increasing the positive bias voltage, the PDI parts become brighter than the OPV units. The bias-dependent contrast changes can be explained by the schematic energy diagrams proposed in Figure 15 which are based upon a number of assumptions: (1) The tunneling junction is asymmetric with the molecules closer to the substrate than to the tip. (2) The interaction between the molecules and the substrate is weak; physisorption does not significantly affect the energy levels of HOMO and LUMO. (3) The molecular orbital that is closer in energy to the Fermi level of the negatively biased electrode (the electron source), affects the tunneling process stronger. (4) OPV and PDI moieties are electronically decoupled or only weakly coupled as indicated by the absorption spectrum.

As depicted in the left scheme, at negative sample bias, the HOMO_{OPV} level is located close to the Fermi level of graphite. Therefore, electrons tunneling from graphite to the tip couple stronger to the HOMO_{OPV} level than to the other energy levels. At high positive bias voltages (right scheme), the LUMO_{PDI} level is closer to the Fermi level of the tip than other states and accordingly is expected to affect the tunneling process, from tip to substrate, to a greater extent. This simplified model is in line with experimental observations: OPV moieties appear brighter (higher tunneling current) at negative sample bias, whereas the PDI moiety appears brighter at high positive sample bias.

Such behavior can also be confirmed by scanning tunneling spectroscopy (STS) measurements,⁷⁵ where the voltage is ramped while the feedback loop is turned off and a current-voltage graph is obtained at a certain position on the substrate. Recently, STS has been used to probe the electronic properties of a multicomponent system which self-assembles into a single-molecule field-effect transistor.⁷⁶

Conclusions and Outlook

STM is more than a tool to make images. It's a powerful methodology to investigate the self-assembly at the liquid/solid and air/solid interface where it provides insight in the ordering, dynamics, reactivity, and electronic properties of the adsorbates. Moreover, it can also act as an active manipulation tool. So far, HOPG has been the substrate of choice but one should move on to other substrates too. Much is to be learned on the effect of the substrate on the self-assembly properties. Use of potential control to direct the self-assembly in a controlled way at the liquid/solid interface will in addition open many more possibilities even for water-insoluble organic compounds.

Acknowledgment. The authors thank the Federal Science Policy through IUAP-V-03, the Institute for the promotion of

innovation by Science and Technology in Flanders (IWT), and the Fund for Scientific Research-Flanders (FWO). S.D.F. is a postdoctoral fellow of FWO. We are very grateful to our many collaborators: Dr. J. van Esch and Prof. B. L. Feringa (Groningen, The Netherlands), Dr. M. Klapper and Prof. K. Müllen (Mainz, Germany), Dr. A. P. H. J. Schenning and Prof. E. W. Meijer (Eindhoven, The Netherlands), Prof. R. Lazzaroni and Prof. J.-L. Brédas (Mons, Belgium), Dr. D. Amabilino and Prof. J. Veciana (Barcelona, Spain), Prof. V. Percec (Pennsylvania, USA), Prof. F. Würthner (Würzburg, Germany), Prof. S. Höger (Karlsruhe, Germany), and Prof. J. van Stam (Karlstad, Sweden) and their co-workers. Finally, we also want to acknowledge our excellent co-workers: Dr. André Gesquière, Dr. Mohamed Abdel-Mottaleb, Dr. Atsushi Miura, Dr. Hiroshi Uji-i, Dr. Wael Mamdouh, and Mr. Matthias Larsson.

References and Notes

- (1) *Handbook of Microlithography, Micromachining, and Microfabrication*; Rai-Choudhury, P., Ed.; SPIE Optical Engineering Press: London, 1997.
- (2) Xia, Y.; Whitesides, G. M. *Angew. Chem., Int. Ed. Engl.* **1998**, *37*, 550.
- (3) Binnig, G.; Rohrer, H.; Gerber, C.; Weibel, E. *Phys. Rev. Lett.* **1982**, *49*, 57.
- (4) Binnig, G.; Quate, C. F.; Gerber, C. *Phys. Rev. Lett.* **1986**, *56*, 930.
- (5) Kim, Y.-T.; Bard, A. J. *Langmuir* **1992**, *8*, 1096.
- (6) Ross, C. B.; Sun, L.; Crooks, R. M. *Langmuir* **1993**, *9*, 632.
- (7) Liu, G.-Y.; Xu, S.; Qian, Y. *Acc. Chem. Res.* **2000**, *33*, 457.
- (8) Müller, W. T.; Klein, D. L.; Lee, T.; Clarke, J.; McEuen, P. L.; Schultz, P. G. *Science* **1995**, *268*, 272.
- (9) Maoz, R.; Cohen, S. R.; Sagiv, J. *Adv. Mater.* **1999**, *11*, 55.
- (10) *Comprehensive supramolecular chemistry*; Atwood, J. L., Davies, J. E. D., Macnicol, D. D., Vogtle, F., Eds.; Pergamon Press: New York, 1996.
- (11) Ulman, A. *Chem. Rev.* **1996**, *96*, 1533 and references therein.
- (12) Bain, C. D.; Whitesides, G. M. *J. Am. Chem. Soc.* **1988**, *110*, 6560.
- (13) Lewis, P. A.; Donhauser, Z. J.; Mantooth, B. A.; Smith, R. K.; Bumm, L. A.; Kelly, K. F.; Weiss, P. S. *Nanotechnology* **2001**, *12*, 231 and references therein.
- (14) Peiner, R. D.; Zhu, J.; Xu, F.; Hong, S. H.; Mirkin, C. A. *Science* **1999**, *283*, 661.
- (15) For an excellent review on self-assembled monolayers and their applications, see: Smith, R. K.; Lewis, P. A.; Weiss, P. S. *Prog. Surf. Sci.* **2004**, *75*, 1.
- (16) Kim, K.; Matzger, A. J. *J. Am. Chem. Soc.* **2002**, *124*, 8772. (b) Plass, K. E.; Kim, K.; Matzger, A. J. *J. Am. Chem. Soc.* **2004**, *126*, 9042.
- (17) McGonical, G. C.; Bernhardt, R. H.; Thomson, D. J. *Appl. Phys. Lett.* **1990**, *57*, 28.
- (18) Rabe, J. P.; Buchholz, S. *Science* **1991**, *253*, 424.
- (19) Yokoyama, T.; Yokoyama, S.; Kamikado, T.; Okuno, Y.; Mashiko, S. *Nature* **2001**, *413*, 619.
- (20) Böhringer, M.; Morgenstern, K.; Schneider, W.-D.; Berndt, R.; Mauri, F.; De Vita, A.; Car, R. *Phys. Rev. Lett.* **1999**, *83*, 324.
- (21) Weckesser, J.; De Vita, A.; Barth, J. V.; Cai, C.; Kern, K. *Phys. Rev. Lett.* **2001**, *87*, 6101.
- (22) Dmitriev, A.; Lin, N.; Weckesser, J.; Barth, J. V.; Kern, K. *J. Phys. Chem. B* **2002**, *106*, 6907.
- (23) Lorenzo, M. O.; Baddeley, C. J.; Murny, C.; Raval, R. *Nature* **2000**, *404*, 376.
- (24) Frommer, J. *Angew. Chem., Int. Ed. Engl.* **1992**, *31*, 1298.
- (25) Cyr, D. M.; Venkataraman, B.; Flynn, G. W. *Chem. Mater.* **1996**, *8*, 1600.
- (26) Giancarlo, L. C.; Flynn, G. W. *Annu. Rev. Phys. Chem.* **1998**, *49*, 297.
- (27) De Feyter, S.; Gesquière, A.; Abdel-Mottaleb, M. M.; Grim, P. C. M.; De Schryver, F. C.; Meiners, C.; Sieffert, M.; Valiyaveetil, S.; Müllen, K. *Acc. Chem. Res.* **2000**, *33*, 8, 520.
- (28) Kunitake, M.; Akiba, U.; Batina, N.; Itaya, K. *Langmuir* **1997**, *13*, 1607.
- (29) He, Y.; Ye, T.; Borguet, E. *J. Am. Chem. Soc.* **2002**, *124*, 11964.
- (30) Yoshimoto, S.; Higa, N.; Itaya, K. *J. Am. Chem. Soc.* **2004**, *126*, 8540.
- (31) Safarowsky, C.; Merz, L.; Rang, A.; Broekmann, P.; Hermann, B. A.; Schalley, C. A. *Angew. Chem., Int. Ed.* **2004**, *43*, 1291.

- (32) Subramanian, S.; Zaworotko, M. J. *Coord. Chem. Rev.* **1994**, *137*, 357. (b) Fan, E.; Vicent, C.; Geib, S. J.; Hamilton, A. D. *Chem. Mater.* **1994**, *6*, 1113. (c) MacDonald, J. C.; Whitesides, G. M. *Chem. Rev.* **1994**, *94*, 2383.
- (33) Zaworotko, M. J. *Chem. Commun.* **2001**, *1*, 1. (b) Alcalá, R.; Martínez-Carrera, S. *Acta Crystallogr.* **1972**, *B28*, 1671. (c) Etter, M. C.; Urbanczyk-Lipkowska, Z.; Jahn, D. A.; Frye, J. S. *J. Am. Chem. Soc.* **1986**, *108*, 5871. (d) Valiyaveetil, S.; Enkelmann, V.; Müllen, K. *J. Chem. Soc., Chem. Commun.* **1994**, 2097. (e) Enkelmann, V.; Valiyaveetil, S.; Moessner, G.; Müllen, K. *Supramol. Sci.* **1995**, *2*, 3. (d) Yang, J.; Marendaz, J.-L.; Geib, S. J.; Hamilton, A. D. *Tetrahedron Lett.* **1994**, *35*, 3665.
- (34) Weckesser, J.; De Vita, A.; Barth, J. V.; Cai, C.; Kern, K. *Phys. Rev. Lett.* **2001**, *87*, 9, 6101.
- (35) Keeling, D. L.; Oxtoby, N. S.; Wilson, C.; Humphry, M. J.; Champness, N. R.; Beton, P. H. *Nano Lett.* **2003**, *3*, 1, 9.
- (36) De Feyter, S.; De Schryver, F. C. *Chem. Soc. Rev.* **2003**, *32*, 3, 139 and references therein.
- (37) Gottarelli, G.; Masiero, S.; Mezzina, E.; Pieraccini, S.; Rabe, J. P.; Samori, P.; Spada, G. P. *Chem. Eur. J.* **2000**, *6*, 17, 3242.
- (38) Buchholz, S.; Rabe, J. P. *Angew. Chem., Int. Ed. Engl.* **1992**, *31*, 189.
- (39) Lei, S. B.; Wang, C.; Yin, S. X.; Wang, H. N.; Wi, F.; Liu, H. W.; Xu, B.; Wan, L. J.; Bai, C. L. *J. Phys. Chem. B* **2001**, *105*, 10838.
- (40) Wintgens, D.; Yablon, D. G.; Flynn, G. W. *J. Phys. Chem. B* **2003**, *107*, *1*, 173.
- (41) De Feyter, S.; Gesquière, A.; Klapper, M.; Müllen, K.; De Schryver, F. C. *Nano Lett.* **2003**, *3*, 1485.
- (42) Gesquière, A.; Jonkheijm, P.; Schenning, A. P. H. J.; Mena-Osteritz, E.; Bäuerle, P.; De Feyter, S.; De Schryver, F. C.; Meijer, E. W. *J. Mater. Chem.* **2003**, *13*, 2164.
- (43) Gesquière, A.; Jonkheijm, P.; Hoebe, F. J. M.; Schenning, A. P. H. J.; De Feyter, S.; De Schryver, F. C.; Meijer, E. W. *Nano Lett.* **2004**, *4*, 1175.
- (44) Jonkheijm, P.; Miura, A.; Zdanowska, M.; Hoebe, F. J. M.; De Feyter, S.; Schenning, A. P. H. J.; De Schryver, F. C.; Meijer, E. W. *Angew. Chem., Int. Ed.* **2004**, *43*, 74.
- (45) Miura, A.; Jonkheijm, P.; De Feyter, S.; Schenning, A. P. H. J.; Meijer, E. W.; De Schryver, F. C. *Small* **2005**, *1*, 131–137.
- (46) Schmidt-Mende, L.; Fechtenkötter, A.; Müllen, K.; Moons, E.; Friend, R. H.; MacKenzie, J. D. *Science* **2001**, *293*, 1119.
- (47) Gesquière, A.; Abdel-Mottaleb, M. M. S.; De Feyter, S.; De Schryver, F. C.; Schoonbeek, F.; van Esch, J.; Kellogg, R. M.; Feringa, B. L.; Calderone, A.; Lazzaroni, R.; Brédas, J. L. *Langmuir* **2000**, *16*, 10385.
- (48) Gesquière, A.; De Feyter, S.; De Schryver, F. C.; Schoonbeek, F.; van Esch, J.; Kellogg, R. M.; Feringa, B. L. *Nano Lett.* **2001**, *1*, 201.
- (49) van Esch, J.; De Feyter, S.; Kellogg, R. M.; De Schryver, F. C.; Feringa, B. L. *Chem. Eur. J.* **1997**, *3*, 1238. (b) De Feyter, S.; Grim, P. C. M.; van Esch, J.; Kellogg, R. M.; Feringa, B. L.; De Schryver, F. C. *J. Phys. Chem. B* **1998**, *102*, 8981.
- (50) De Feyter, S.; Larsson, M.; Schuurmans, N.; Verkuijl, B.; Zorinians, G.; Gesquière, A.; Abdel-Mottaleb, M. M.; van Esch, J.; Feringa, B. L.; van Stam, J.; De Schryver, F. C. *Chem. Eur. J.* **2003**, *9*, 1198.
- (51) De Feyter, S.; Larsson, M.; Gesquière, A.; Verheyen, H.; Louwet, F.; Groenendaal, B.; van Esch, J.; Feringa, B. L.; De Schryver, F. C. *ChemPhysChem* **2002**, *11*, 966.
- (52) Abdel-Mottaleb, M. M. S.; De Feyter, S.; Sieffert, M.; Klapper, M.; Müllen, K.; De Schryver, F. C. *Langmuir* **2003**, *19*, 8256.
- (53) Gesquière, A.; Abdel-Mottaleb, M. M. S.; Sieffert, M.; Müllen, K.; De Schryver, F. C. *Langmuir* **1999**, *15*, 6821.
- (54) Mamdoui, W.; Uji-i, H.; Dulcey, A. E.; Percec, V.; De Feyter, S.; De Schryver, F. C. *Langmuir* **2004**, *20*, 7678.
- (55) Abdel-Mottaleb, M. M. S.; Schuurmans, N.; De Feyter, S.; van Esch, J.; Feringa, B. L.; De Schryver, F. C. *Chem. Commun.* **2002**, 1894.
- (56) De Feyter, S.; Abdel-Mottaleb, M. M. S.; Schuurmans, N.; Verkuijl, B.; van Esch, J.; Feringa, B. L.; De Schryver, F. C. *Chem. Eur. J.* **2004**, *10*, 1124.
- (57) Enkelmann, V. *Adv. Polym. Sci.* **1984**, *63*, 91.
- (58) Grim, P. C. M.; De Feyter, S.; Gesquière, A.; Vanoppen, P.; Rucker, M.; Valiyaveetil, S.; Moessner, G.; Müllen, K.; De Schryver, F. C. *Angew. Chem., Int. Ed. Engl.* **1997**, *36*, 2601.
- (59) Okawa, Y.; Aono, M.; *Nature* **2001**, *409*, 683. (b) Okawa, Y.; Aono, M. *J. Chem. Phys.* **2001**, *115*, 2317.
- (60) Miura, A.; De Feyter, S.; Abdel-Mottaleb, M. M. S.; Gesquière, A.; Grim, P. C. M.; Moessner, G.; Sieffert, M.; Klapper, M.; Müllen, K.; De Schryver, F. C. *Langmuir* **2003**, *19*, 6474.
- (61) Akai-Kasaya, M.; Shimizu, K.; Watanabe, Y.; Saito, A.; Aono, M.; Kuwahara, Y.; *Phys. Rev. Lett.* **2003**, *91*, 255501.
- (62) Endo, O.; Ootsubo, H.; Toda, N.; Suhara, M.; Ozaki, H.; Mazaki, Y. *J. Am. Chem. Soc.* **2004**, *126*, 9894.
- (63) Barlow, S. M.; Raval, R. *Surf. Sci. Rep.* **2003**, *50*, 201.
- (64) Stevens, F.; Walba, D. M.; Clark, N. A.; Parks, D. C. *Acc. Chem. Res.* **1996**, *29*, 591 and references therein. (b) De Feyter, S.; Grim, P. C. M.; Rucker, M.; Vanoppen, P.; Meiners, C.; Sieffert, M.; Valiyaveetil, S.; Müllen, K.; De Schryver, F. C. *Angew. Chem., Int. Ed. Engl.* **1998**, *37*, 1223. (c) De Feyter, S.; Gesquière, A.; Grim, P. C. M.; De Schryver, F. C.; Valiyaveetil, S.; Meiners, C.; Sieffert, M.; Müllen, K. *Langmuir* **1999**, *15*, 2817. (d) Giancarlo, L. G.; Flynn, G. W. *Acc. Chem. Res.* **2000**, *33*, 491 and references therein.
- (65) Qian, P.; Nanjo, H.; Yokoyama, T.; Suzuki, T. M. *Chem. Lett.* **1998**, 1133. (b) Fang, H. B.; Giancarlo, L. C.; Flynn, G. W. *J. Phys. Chem. B* **1998**, *102*, 7311. (c) Qian, P.; Nanjo, H.; Yokoyama, T.; Suzuki, T. M.; Akasaka, K.; Orhui, H. *Chem. Commun.* **2000**, 2021. (d) Ohtani, B.; Shintani, A.; Uosaki, K. *J. Am. Chem. Soc.* **1999**, *121*, 6515. (e) Lorenzo, M. O.; Baddelley, C. J.; Muryn, C.; Raval, R. *Nature* **2000**, *404*, 376. (f) Chen, Q.; Frankel, D. J.; Richardson, N. V. *Surf. Sci.* **2002**, *497*, 37. (g) Xu, Q.-M.; Wang, D.; Wan, L.-J.; Wang, C.; Bai, C.-L.; Feng, G.-Q.; Wang, M.-X. *Angew. Chem., Int. Ed.* **2002**, *41*, 3408. (h) Fasel, R.; Parschau, M.; Ernst, K.-H. *Angew. Chem., Int. Ed.* **2003**, *42*, 5178. (i) Kühnle, A.; Linderoth, T. R.; Besenbacher, F. *J. Am. Chem. Soc.* **2003**, *125*, 14680.
- (66) Yoneya, M.; Yokoyama, H. *J. Chem. Phys.* **2001**, *114*, 9532.
- (67) Pérez-García, L.; Amabilino, D. B. *Chem. Soc. Rev.* **2002**, *31*, 342.
- (68) De Feyter, S.; Gesquière, A.; Wurst, K.; Amabilino, D. B.; Veciana, J.; De Schryver, F. C. *Angew. Chem., Int. Ed.* **2001**, *40*, 3217.
- (69) Mamdoui, W.; Uji-i, H.; Gesquière, A.; De Feyter, S.; Amabilino, D. B.; Abdel-Mottaleb, M. M. S.; Veciana, J.; De Schryver, F. C. *Langmuir* **2004**, *20*, 9628.
- (70) Stabel, A.; Rabe, J. *Angew. Chem., Int. Ed. Engl.* **1995**, *34*, 1609. (b) Tchegbotareva, N.; Yin, X.; Watson, M. D.; Samori, P.; Rabe, J. P.; Mullen, K. *J. Am. Chem. Soc.* **2003**, *125*, 9734. (c) Lackinger, M.; Müller, T.; Gopakumar, T. G.; Müller, F.; Hietschold, M.; Flynn, G. W. *J. Phys. Chem. B* **2004**, *108*, 2279.
- (71) Smith, D. P. E.; Hörber, J. K. H.; Binnig, G.; Nejo, H. *Nature* **1990**, *334*, 641. (b) Rabe, J. P.; Buchholz, S.; *Phys. Rev. Lett.* **1991**, *66*, 2096. (c) Rabe, J. P.; Buchholz, S.; Askadskaya, L. *Synth. Metals* **1993**, *54*, 339. (d) Stabel, A.; Dasaradhi, L.; O'Hagan, D.; Rabe, J. P. *Langmuir* **1995**, *11*, 1427. (e) Venkataram, B.; Flynn, G. W.; Wilbur, J.; Folkers, J. P.; Whitesides, G. M. *J. Phys. Chem.* **1995**, *99*, 8684. (f) Cyr, D. M.; Venkataraman, B.; Flynn, G.; Black, A.; Whitesides, G. M. *J. Phys. Chem.* **1996**, *100*, 13747. (g) Giancarlo, L.; Cyr, D.; Muyskens, K.; Flynn, G. W. *Langmuir* **1998**, *14*, 1465. (h) Claypool, C. L.; Faglioni, F.; Goddard, W. A., III; Gray, H. B.; Lewis, N. S.; Marcus, R. A. *J. Chem. Phys. B* **1997**, *101*, 5978.
- (72) Crystal, J.; Zhang, L. Y.; Friesner, R. A.; Flynn, G. W. *J. Phys. Chem. A* **2002**, *106*, 1802. (b) Faglioni, F.; Claypool, C. L.; Lewis, N. S.; Goddard, W. A. *J. Phys. Chem. B* **1997**, *101*, 5996. (c) Lazzaroni, R.; Calderone, A.; Brédas, J. L.; Rabe, J. P. *J. Chem. Phys.* **1997**, *107*, 1, 99. (d) Scudiero, L.; Barlow, D. E.; Hipps, K. W. *J. Phys. Chem. B* **2002**, *106*, 996 and references cited in these papers.
- (73) Schmickler, W. *J. Electroanal. Chem.* **1990**, *296*, 283. (b) Fischer, A. J.; Blöchl, P. E. *Phys. Rev. Lett.* **1993**, *70*, 3263. (c) Tao, N. J. *Phys. Rev. Lett.* **1996**, *76*, 21, 4066. (d) Barlow, D. E.; Hipps, K. W. *J. Phys. Chem. A* **2000**, *104*, 5993. (e) Han, W.; Durantini, E. N.; Moore, T. A.; Moore, A. L.; Gust, D.; Rez, P.; Leatherman, G.; Seely, G. R.; Tao, N.; Lindsay, S. M. *J. Phys. Chem. B* **1997**, *101*, 10719.
- (74) Miura, A.; Chen, Z.; De Feyter, S.; Zdanowska, M.; Uji-i, H.; Jonkheijm, P.; Schenning, A. P. H. J.; Meijer, E. W.; Würthner, F.; De Schryver, F. C. *J. Am. Chem. Soc.* **2003**, *125*, 14968.
- (75) Jäckel, F.; Wang, Z.; Watson, M. D.; Müllen, K.; Rabe, J. P. *Chem. Phys. Lett.* **2004**, *387*, 372.
- (76) Jäckel, F.; Watson, M. D.; Müllen, K.; Rabe, J. P. *Phys. Rev. Lett.* **2004**, *92*, 188303.